Accelerated Greenland ice sheet mass loss under high greenhouse gas forcing as simulated by the coupled CESM2.1-CISM2.1

Laura Muntjewerf[1], Raymond Sellevold[1], Miren Vizcaino[1], Carolina Ernani da Silva[1], Michele Petrini[1], Katherine Thayer-Calder[2], Meike D. W. Scherrenberg[1], Sarah L. Bradley[3], Jeremy Fyke[4], William H. Lipscomb[2], Marcus Lofverstrom[5], William J. Sacks[2]

[1]Department of Geoscience and Remote Sensing, Delft University of Technology, Delft, The Netherlands

[2]Climate and Global Dynamics Laboratory, National Center for Atmospheric Research, Boulder, CO, USA

[3]Department of Geography, The University of Sheffield, Sheffield, UK

[4]Associated Engineering Group Ltd., Calgary, AB, Canada

[5]Department of Geosciences, University of Arizona, Tucson, AZ, USA

Key Points:

- 1% per year increase in CO_2 results in global warming of 5.2 K at 4×pre-industrial levels, and 8.5 K after 210 years stabilization.
- The corresponding GrIS contribution to global mean sea level rise is 107 mm SLE, and 1140 mm SLE, respectively.
- The accelerated mass loss is mainly driven by the SMB, where the ice-albedo feedback provides the additional melt energy.

Corresponding author: L. Muntjewerf, `L.Muntjewerf@tudelft.nl`

Abstract

The Greenland ice sheet (GrIS) has been losing mass in the last several decades, and is currently contributing around 0.7 mm sea level equivalent (SLE) yr^{-1} to global mean sea level rise (SLR). As ice sheets are integral parts of the Earth system, it is important to gain process-level understanding of GrIS mass loss. This paper presents an idealized high-forcing simulation of 350 years with the Community Earth System Model version 2.1 (CESM2.1) including interactively coupled, dynamic GrIS with the Community Ice Sheet Model v2.1 (CISM2.1). From pre-industrial levels (287 ppmv), the CO_2 concentration is increased by 1% yr^{-1} till quadrupling (1140 ppmv) is reached in year 140. After this, the forcing is kept constant. Global mean temperature anomaly of 5.2 K and 8.5 K is simulated by years 131–150 and 331-150, respectively. The North Atlantic Meridional Overturning Circulation strongly declines, starting before GrIS runoff substantially increases. The projected GrIS contribution to global mean SLR is 107 mm SLE by year 150, and 1140 mm SLE by year 350. The accelerated mass loss is driven by the SMB. Increased long-wave radiation from the warmer atmosphere induces an initial slow SMB decline. An acceleration in SMB decline occurs after the ablation areas have expanded enough to trigger the ice-albedo feedback. Thereafter, short-wave radiation becomes an increasingly important contributor to the melt energy. The turbulent heat fluxes further enhance melt and the refreezing capacity becomes saturated. The global mean temperature anomaly at the start of the accelerated SMB decline is 4.2 K.

Plain Language Summary

The Greenland ice sheet (GrIS) has been losing mass in the last decades, contributing to global mean sea level rise (SLR). Ice sheets are an integral part of the complex Earth system. To understand what drives the GrIS mass loss, the Earth system as a whole must be considered.

With an Earth system model that includes GrIS ice flow, this study addresses: 1) the extent to which the GrIS responds to increased atmospheric warming, and 2) the main processes that govern this response. The model is forced with an idealized greenhouse gas scenario: the atmospheric CO_2 concentration is increased by 1% per year till quadrupling (1140 ppmv). After this, the forcing is kept constant for another two centuries.

The GrIS reacts nonlinearly to warming. The global mean temperature increases with 5.2 K until CO_2 quadrupling, and the GrIS contributes 107 mm sea level equivalent (SLE) per year to global mean SLR. After two centuries after CO_2 stabilisation, global warming further increases to 8.5 K. The GrIS contribution to SLR increases tenfold, to 1140 mm SLE. The accelerated mass loss is driven by an increasingly negative surface mass balance. The ice-albedo feedback supplies the additional energy for this melt acceleration.

1 Introduction

The Greenland ice sheet (GrIS) is the largest freshwater reservoir in the Northern Hemisphere, storing 7.4 m potential global mean sea level rise (SLR) (Bamber et al., 2013; Morlighem et al., 2017). Between 2007 and 2017, the GrIS has been contributing to the global mean SLR at a rate of 0.7 mm sea level equivalent (SLE) yr^{-1} (Shepherd et al., 2019), as a result of increased surface melt, runoff, and ice discharge to the ocean (van den Broeke et al., 2016). Future GrIS contribution to global mean SLR is expected to further increase, with great uncertainty ranges (Bamber et al., 2019).

Ice sheets are integral components of the Earth system, which are sensitive to climate change, and influence climate through changes in topography, albedo, and freshwater fluxes to the ocean (J. Fyke et al., 2018). A selection of important ice-sheet/atmospheric feedbacks and interactions include: the elevation feedback on melt (Oerlemans, 1981; Edwards et al., 2014), the ice/albedo feedback (Box et al., 2012), the coupling between the surface mass balance (SMB) and ice discharge (Lipscomb et al., 2013; Goelzer et al., 2013), and effects of orographic change on atmospheric circulation (Ridley et al., 2005).

Coupled Earth system/ice sheet models are required to gain further understanding of how GrIS mass loss is governed by these patterns of interaction. Much effort has been undertaken in this area of research, and overviews of progress have been continuously documented (Pollard, 2010; Vizcaino, 2014; Goelzer et al., 2017; Rybak et al., 2018; Hanna et al., 2020). Vizcaíno et al. (2013); Alexander et al. (2019) highlight the importance of an SMB calculation based on the surface energy balance; melt parameterizations based on temperature are not sufficient in order to simulate the feedbacks and interactions in a changing climate in a physically realistic way. The accuracy of the SMB calculation in an Earth system model (ESM) depends on the snow physics parameterization (van Kampenhout et al., 2017), the albedo parameterization (Helsen et al., 2017), and model resolution (Gregory & Huybrechts, 2006; Lofverstrom & Liakka, 2018; van Kampenhout et al., 2019). Further, the computational demand of coupling large-scale climate processes with local-scale ice sheet processes, combined with the long response time of ice sheets, is an additional challenge (Vizcaino et al., 2015).

Taking on this challenge, the Community Ice Sheet Model version 2.1 (CISM2.1) has recently been included as an interactive component in the Community Earth System Model 2.1 (CESM2.1). The model includes bi-directional coupling of the ice sheet with the land and atmosphere through an energy-based calculation of surface melt, downscaling through elevation classes to the ice sheet model grid (Lipscomb et al., 2013; Sellevold et al., 2019), and dynamic ice sheet topography and glacier cover (Muntjewerf et al., in preparation). As ocean/ice sheet feedbacks are currently less well understood (J. Fyke et al., 2018) and the GrIS has relatively little interaction with the ocean, the model coupling is limited to one-way coupling at the ice sheet/ocean interface: the GrIS provides fresh water fluxes to the ocean but the ocean does not provide forcing to the calving fronts.

This paper presents the results of a multi-century (350-year) simulation of GrIS evolution under an idealized CO_2 scenario. The forcing protocol starts with a 140-year transient period where the atmospheric CO_2 concentration increases by 1% per year, followed by a period (210 years) where the high CO_2 concentration is kept constant. The goal of this experiment design is to gain process-level understanding of GrIS mass loss. This includes assessing the timing and magnitude of the GrIS response in relation to the global climate response, and the relative importance of the processes that regulate GrIS behavior. Further, we investigate non-linearities in the sensitivity to the forcing, and apparent accelerations and tipping points in the GrIS contribution to SLR.

Section 2 describes the coupled model CESM2.1-CISM2.1 and the experimental set-up. The main results are analysed in section 3, and section 4 contains a discussion and conclusions.

2 Method: Model Description and Experimental Set-Up

2.1 Model Description

Model simulations were carried out with the Community Earth System Model version 2.1 (CESM2.1) (Danabasoglu et al., accepted pending minor revisions), which is a fully coupled, global Earth system model with prognostic components for atmosphere, ocean, land, sea-ice, and land-ice. CESM2 is one of the models contributing to the Coupled Model Intercomparison Project phase 6 (CMIP6, Eyring et al. (2016)), and the Ice Sheet Model Intercomparison Project for CMIP6 (ISMIP6, Nowicki et al. (2016)). Atmospheric processes are simulated with the Community Atmosphere Model version 6, using the finite volume dynamical core (CAM6-FV, Lin and Rood (1997); Neale and Coauthors (in review)), at a nominal 1° horizontal grid, and 32 levels in the vertical. Ocean processes are simulated with the Parallel Ocean Program version 2 (POP2, Smith et al. (2010)), which runs on a nominal 1° displaced-pole grid with 60 levels in the vertical. Sea-ice is represented by the Los Alamos National Laboratory sea-ice model, version 5 (CICE5, Hunke et al. (2017)), which runs on the same horizontal grid as POP2.

Land processes are simulated by the Community Land Model version 5 (CLM5, Lawrence et al. (2019)). CLM5 has the same horizontal grid as CAM6; a nominal 1° (0.90° latitude$\times$1.25° longitude) grid. Depending on land surface type, there is a maximum 15 subsurface layers with layer depth ranging from $\sim$0.02 m near the surface to $\sim$14 m for the deepest layer. Snow is represented by up to 10 snow layers with a maximum depth of 10 m water equivalent. CLM5 further includes the Model for Scale Adaptive River Transport (MOSART) to handle land surface runoff based on gradients of topography.

The Greenland ice sheet (GrIS) is simulated using the Community Ice Sheet Model version 2.1 (CISM2.1, Lipscomb et al. (2019)). For the GrIS, CISM runs on a 4 km rectangular grid with 11 terrain-following vertical levels. The velocity solver uses a depth-integrated higher-order approximation (Goldberg, 2011) of the Stokes equations for ice flow. A pseudo-plastic sliding law described by Aschwanden et al. (2016) is used to parameterize basal sliding; Bradley et al. (in preparation) analyze CISM2.1 sensitivity to basal sliding parameters in standalone multi-millenial simulations. Calving in this study is parameterized via the flotation criterion, where all floating ice is immediately discharged to the ocean.

2.2 Coupling Description

In the default CESM2 configuration, ice sheets do not evolve, but the simulations described here have a dynamic GrIS, which is interactively coupled to other Earth system components. CESM2.1-CISM2.1 has a time evolving Greenland ice sheet that is interactively coupled to the other Earth system components (Muntjewerf et al., in preparation). The model features an SMB calculation with a surface-energy-balance calculation of melt. The SMB is computed in CLM5 in multiple elevation classes for each glaciated grid cell (Lipscomb et al., 2013; Sellevold et al., 2019), with interactive coupling to CAM6 and explicit modelling of albedo, refreezing, and snow and firn compaction (van Kampenhout et al., 2017; Van Kampenhout et al., accepted). The SMB is then downscaled by the coupler to the higher-resolution CISM2 grid using a trilinear remapping scheme, corrected to conserve global water mass. The remapping scheme is described in Muntjewerf et al. (in preparation).

The Greenland freshwater budget from surface runoff, basal melt, and ice discharge (i.e., calving) is coupled to the ocean model. The freshwater flux received by POP2 from the GrIS is the sum of surface runoff from CLM5, and basal melt and ice discharge from CISM. Surface runoff is routed to the ocean via MOSART based on topographic gradients. In the ocean, this flux together with basal melt computed from CISM are distributed by an estuary box model over the 30 m upper vertical layers of the grid cell (Sun et al., 2017). Ice discharge as calculated by CISM is delivered to the nearest ocean grid cell and spread horizontally in the surface layer with a Gaussian distribution and maximum distance of 300 km, where it is melted instantaneously.

CESM2.1-CISM2.1 further includes dynamic land-unit change from glaciated to vegetated land cover as the ice sheet retreats, or vice versa when the ice sheet advances. The ice sheet surface topography from CISM is used to recompute the fractional glacier coverage in CLM5, subsequently affecting the albedo and soil and vegetation characteristics. The evolving ice-sheet topography is also coupled to the atmosphere model, which enables orographic circulation feedbacks. Surface elevation and surface roughness fields of CAM6 are updated every 10 years in the simulations of this study.

2.3 Experimental Set-Up

Two simulations are analyzed in this study: a 300-year control simulation of the pre-industrial era (year 1850 CE), and a 350-year transient simulation with an idealized atmospheric CO_2 scenario. The atmospheric CO_2 concentration initially increases by 1% per year until reaching a 4x pre-industrial CO_2 level (1140 ppmv; hereafter 4xCO_2) in year 140. The 4xCO_2 level is then maintained for the remaining 210 years of the simulation. These simulations are part of ISMIP6, and the simulation data is openly accessible. Further details on the forcing scenarios are provided by Eyring et al. (2016), and details on the experimental set-up are provided by Nowicki et al. (2016).

Both simulations start from the spun-up pre-industrial Earth system/ice sheet state in Lofverstrom et al. (in review). A near-equilibrium state is obtained by alternating between a fully coupled model configuration, and a computationally efficient (coupled) model configuration with a data atmosphere; see Lofverstrom et al. (in review) for a full description of the method. The residual drift in the near-equilibrated GrIS volume is 0.03 mm SLE yr^{-1}, with a GrIS volume and area overestimate of 12% and 15%, respectively. Ice sheet velocities and SMB compare reasonably well with present-day observations and regional modelling reconstructions.

3 Results

We refer to the years 131–150 (around the time the model reaches $4xCO_2$) as "stabilization", and years 331–350 as "end-of-simulation"; shaded blue in the (Figure 1a).

3.1 Global, Arctic and North Atlantic Climate Change

3.1.1 Global and Regional Climate Change

The evolution of the cumulative top-of-the-atmosphere (TOA) radiation imbalance is shown in Figure 1b: increasingly more radiation is kept in the Earth System. Therefore, the system warms. The global annual average near-surface temperature increases at an approximately constant rate in the first 140 model years. By stabilization, the warming is 5.2 K (σ=0.3 K) (Figure 1c). In the two centuries that follow, the temperature increases by an additional 3.3 K. Arctic temperatures (Arctic is here defined as north of 60°N) follow a similar trajectory. The polar amplification (ratio between Arctic and global temperature increase) is 1.6, with much of the signal coming from summer sea-ice loss. The GrIS amplification (ratio between GrIS and global temperature increase) with 1.1 is much smaller than the Arctic amplification, as the GrIS is a terrestrial region with a perennial ice/snow cover that holds the summer surface temperature below melt point.

Spatially, the annual near-surface temperature increases globally (Figure 1d), with the most pronounced warming (> 18 K) in the Arctic basin, the Canadian archipelago, and Antarctica. The North Atlantic warms the least, in connection with changes in the ocean circulation and associated meridional heat transport (see section 3.1.2). The Arctic becomes seasonally-ice free before the end of the first century (Figure S1), and almost completely ice-free from year 270, as the March sea-ice extent declines to less than 2×10^6 km^2.

The zonal means of near-surface summer and winter temperatures are shown in Figure 2. The high Arctic ($> 80°$N) at stabilization warms somewhat less than lower Northern Hemisphere latitudes. This is possibly connected with widespread melting of the decreasing sea-ice cover. By end-of-simulation, the high Arctic warms more than other Northern Hemisphere latitudes due to lack of sea-ice and a generally reduced snow cover. The summer warming on the rest of the globe is latitudinally uniform. The interior of the GrIS is the only region in the Northern Hemisphere where the near-surface temperatures remain below freezing throughout the summer months by end-of-simulation (Figure 2b).

The zonally averaged near-surface temperature in Northern Hemisphere winter (Figure 2c) shows the polar amplification for 131–150 and 331–350. The meridional temperature gradient reverses from $\sim 70°$N in both periods, though more pronounced in the second period. This reversal reflects the sea-ice thinning and retreat by 131–150, and sea-ice-free conditions by 331–350, given the Arctic land-ocean distribution. By end-of-simulation, most Arctic land regions remain below freezing temperatures in boreal winter, while the ocean is nearly free of sea-ice (Figure S1 and Figure 2d). The GrIS, however, is the coldest region in Northern Hemisphere, this climatic signature of the GrIS by 331–350 is illustrated in Figure 2c.

3.1.2 Changes in Ocean Circulation

The North Atlantic Meridional Overturning circulation (NAMOC) weakens significantly during the first 150 years (Figure 3a). The NAMOC index — defined here as the maximum of the overturning stream function north of 28°N and below 500 m depth — decreases at a rate of about 0.12 Sv yr^{-1} until year 140, and by 0.06 Sv yr^{-1} between 140 and 170, reaching values below 6 Sv. The thickness of the upper, poleward moving branch of the overturning cell decreases by 1 km by stabilization (Figure 3b). By end-of-simulation, the location of the maximum overturning has migrated equatorward by four degrees, and is 250 m shallower (Supplementary Table 1).

Figure 3a shows the simulated evolution of the mean January-February-March mixed layer depth (MLD) in the deep convection regions in the Labrador Sea, Irminger Sea, Iceland Basin, and Barents Sea The Denmark Strait and Faroe Bank overflows are located in the latter two regions. The mixed layer in all regions becomes drastically shallower in the first 100 years of the simulation. The Labrador Sea is the first region where the MLD reaches the threshold of 100 m, which indicates negligible deep convection. Next, the deep convection stops in the Irminger Sea, Iceland Basin and Barents Sea. By the time this threshold is reached in all four regions (year 150), the NAMOC Index has weakened to 5.6 Sv.

3.2 GrIS Contribution to Sea Level Rise

The simulated pre-industrial GrIS is close to equilibrium with a global mean SLR contribution of 0.03 mm SLE yr^{-1} and a relatively large standard deviation of 0.23 mm SLE yr^{-1} over the 300 years of simulation (Table 1). The behaviour of the mass loss in the 1% simulation can be separated into three distinctly different periods (Table S2). First, the GrIS responds slowly, and the mass loss increases at a rate of 2.4 Gt yr^{-2} in the years 1–119. The modern observed mass loss ($\sim$ 0.7 mm SLE yr^{-1}, Shepherd et al. (2019)) is reached in the first years of the second century. Then, from year 120 at a global warming of 4.2 K, the mass loss accelerates at 11.3 Gt yr^{-2} until year 225. The average SLR contribution in the years 131–150 is 764 Gt yr^{-1} (+2.2 mm SLE yr^{-1}) (Figure 4b, black line). Finally, the mass loss decelerates with approximately -4.6 Gt yr^{-2} (0.01 mm SLE yr^{-2})(years 226-350). The average mass loss rate begins to stabilizes around -2350 Gt yr^{-1} (+6.6 mm SLE yr^{-1}) in the years 331–350. The overall increase in annual mass loss results in a cumulative contribution of 107 mm SLE by year 140, and 1140 mm SLE by the end of the simulation (Figure 4a). The GrIS mass budget components (SMB and dynamic ice discharge) are discussed in Sections 3.3 and 3.4. The basal melt rate is further excluded from the discussion, as CESM2 does not simulate ice shelves and thus no sub-shelf melting; therefore the basal mass balance has a very small contribution to the total mass budget.

3.3 Change in Surface Mass Balance

The SMB in the pre-industrial is 585 Gt yr^{-1} (Table 1), which is higher than present day SMB (Noël et al., 2015, 2016; Fettweis et al., 2017), primarily due to a larger ice sheet and overestimated snowfall rates (Lofverstrom et al., in review; Van Kampenhout et al., accepted). In the 1% simulation, the surface mass loss increases by three distinct rates over within these time periods (Figure 4b, orange line), similar to the total mass loss behaviour in Section 3.2. SMB changes by -3.5 Gt yr^{-2} until year 119, by -13.9 Gt yr^{-2} for the period 120-226, and by -5.4 Gt yr^{-2} during 226-350 (Table S2). The anthropogenic signal in the SMB emerges over background variability by year 84 (following the primary criterion in J. G. Fyke et al. (2014)). At this year, the global mean temperature anomaly is 2.5 K. The SMB becomes negative by year 96, at a warming of 2.9 K.

Figure S2 provides the evolution of the percentage ablation area as a function of the time-dependent GrIS area (note that the GrIs area is decreasing). The ablation area is the area with average SMB < 0. In the pre-industrial simulation, the ablation area is 5.5% (1.1×10^5 km^2). The ablation areas expand rapidly (Figure S2), with three distinct trends whose timing is different from that of the SMB trends. Up to year 98, the ablation area expands at a rate of 0.1% yr^{-1}. The anthropogenic-forced signal emerges from background variability in year 46, when the global mean temperature anomaly is 1.1 K. In a CESM2.1-only simulation (without an interactive ice sheet) under the same scenario forcing (Sellevold & Vizcaino, submitted), this ablation-area signal emerges sooner than the SMB signal due to lower variability. From year 99, the rate of expansion triples to 0.3% yr^{-1}; by years 131–150, the ablation area is 24.2% (4.8×10^5 km^2). Between years 193–350, the trend is again 0.1% yr^{-1}, and by end-of-simulation, the ablation area is 60.1% (10.1×10^5 km^2).

Figure 5 shows the time evolution of the SMB components (Figure 5). Total precipitation rate increases over the course of the simulation (Figure 5, Table 2), but the signal emerges relatively late (year 202, for a global mean temperature increase of 6.8 K). This is due to the combination of global warming and reduced NAMOC signals (Figures 1 and 3) in the Greenland region, with the latter reducing the precipitation in the southern part of the ice sheet and partly compensating the moderate precipitation increases elsewhere (Sellevold & Vizcaino, submitted). Snowfall, unlike precipitation, decreases during the simulation, but does not emerge over background variability. This decrease is due to an increased fraction of precipitation falling as rain, as a result of warming (from 9% pre-industrial to 39% by end-of-simulation). More detailed analysis with spatial maps is made for a 150-year CESM2.1-only simulation under the same scenario forcing but with prescribed GrIS topography (Sellevold & Vizcaino, submitted).

Melt increases from the beginning of the simulation and accelerates after the first century. By stabilization, the melt is five times greater than the pre-industrial melt (Table 3). Melt continues to increase until year 280, and reaches nine times the pre-industrial value by the end of simulation. Refreezing increases from the start of simulation. This is mostly due to increased available liquid water from surface melt and rainfall, with melt representing the largest contribution (90% by end-of-simulation). The refreezing capacity, defined as the fraction of refreezing to available melt water, decreases from 46% pre-industrial (in agreement with estimates from RACMO, Noël et al. (2018)) to 32% (131–150), in agreement with RCP8.5 projections (van Angelen et al., 2013). After stabilization, the refreezing amount stops increasing, despite further increase in available water. This is presumably because the capacity of snow to store meltwater is saturated. From year 200 to end-of-simulation refreezing rates decrease. By end-of-simulation, the refreezing capacity is 13%. The maximum refreezing has values close to but below the total snowfall rate (93% for 131–150, and 79% for 331–350), confirming the validity of parameterizations that estimate potential refreezing as a fraction of total snowfall (Aschwanden et al., 2019).

The surface energy balance components (Figure 5b) are necessary to explain the melt acceleration after year 120 (Figure 5a), and the subsequent acceleration in SLR contribution (Figure 4a) In the first century of simulation, the primary source of additional melt energy is the increase in net long-wave radiation (Figure 5b, Table 2). The net short-wave radiation at the surface does not increase, because reduced incoming radiation from enhanced cloudiness (Sellevold & Vizcaino, submitted) cancels out with reduced reflected short-wave as the surface albedo decreased from the initial melt increase. By stabilization, the primary source of melt (40% of total) is still long-wave radiation. By end-of-simulation, decreases in albedo make solar radiation the primary source (39%), followed by the turbulent fluxes (34%).

A threshold or tipping point in the melt energy is reached close to year 120. The net solar and turbulent heat fluxes substantially increase, while the net long-wave radiation continues a more smooth increase, as the global atmosphere continues warming (Figure 1). The former (abrupt) increases are the result of the combination of two processes. On the one hand, the ice-albedo feedback is triggered and amplifies the melt increase as the ablation area expands (Figure S2). On the other hand, the global mean temperature increase exceeds a certain threshold (4.2 K) that is regionally translated into summer GrIS mean temperatures close to the melting point (Table 2). Large parts of the ice sheet surface are at melting point, while near-surface temperatures can above the melting point. This results in a stronger surface temperature inversion and associated enhanced turbulent fluxes. Section 3.6 further examines the spatial extent of changes in the Greenland summer climate.

3.4 Change in Ice flow and Discharge

3.4.1 Map of Mass Loss and Velocity Changes

Figures 6 and S3 show the spatial distribution of the mass loss and its components, as well as the change in surface velocities. Most of the ice sheet thins below the 2,000 m elevation contour, and all the ice sheet thins below 2,500 m, by years 131–150 (Figure 6b) and 331–350 (Figure 6c), respectively, as a result of expansion of the ablation area and increase in flow (Figure 6h,i) from the interior toward the margins. The ice sheet thickens somewhat in the interior, as a result of local increases in snowfall from an enhanced hydrological cycle (spatial maps of changes in snowfall and precipitation are presented in Sellevold and Vizcaino (submitted)). As a result of the thinning pattern, the slope angle increases substantially where the ablation and accumulation zones meet. This causes an increase in the driving stress that results in higher velocities in the transition area from the high interior and the rapidly thinning low elevation margins. While faster flow partly reduces mass loss at the margins as ice advection from the interior increases, it favors upward migration of the equilibrium line and thinning upstream (e.g., Vizcaino et al. (2015)). The gross pattern of SMB, velocity, and thickness change by stabilization is similar to the results by 2081-2100 under the SSP5-8.5 scenario (Muntjewerf et al., submitted), when the atmospheric CO_2 concentration is similar. The SSP5-8.5, however, reaches a more negative SMB (-565 Gt yr^{-1} versus -367 Gt yr^{-1}) due to a stronger increase in CO_2 forcing relatively late in the simulation.As the ice sheet margins thin and retreat, the velocities of outlet glaciers decrease, resulting in almost 200 Gt yr^{-1} lower discharge by years 131–150 (Table 1, Figure S3). By end-of-simulation, ice sheet retreat results in a generally terrestrial margin in all basins. The northwestern outlet glacier termini become terrestrial, and discharge exceeding 5 Gt yr^{-1} is occurring only in Jakobshavn, Peterman, Helheim, Kangerlussuaq, and the North East Greenland Ice Stream NEGIS).

3.4.2 Changes in Major Outlet Glaciers

In order to further analyze the simulated change at the GrIS margins, the flowline sections of seven major outlet glaciers draining different GrIS basins are examined: Nioghalvfjerdsfjord Gletscher and Zachariae Isstrøm1,2 in the northeast (NE) basin, Petermann Gletscher and Humboldt Gletscher in the north (NO) basin, Kangerlussuaq Gletscher and Helheim Gletscher in the southeast (SE) basin, and Jakobshavn Isbræ in the central-west (CW) basin. Figure S4 gives the location of these flowlines, as well as the timing of margin retreat and the comparison between surface velocity maps at pre-industrial and end-of-simulation.

In the southeast basin, the margins of Kangerlussuaq and Hellheim Gletschers do not retreat during the simulation (Figure 7, Supplementary Table 3). At year 140, the SMB is still positive over a large portion of the glaciers. At this time, only the lower part of the glaciers has a negative SMB, with a rapid downstream decline and values as low as -1.5 m yr^{-1} at the glacier terminus. A nearly identical, relatively steep downstream SMB gradient is simulated until year 350, when values range from -0.5 m yr^{-1} inland to -2.5 m yr^{-1} at the glacier terminus. At the beginning of the simulation, ice velocity is higher than 2 km yr^{-1} in regions with steep bedrock topography. During this time, in Hellheim Gletscher the ice velocity increases smoothly from 1 to 4 km yr^{-1} in the lower part of the glacier. Similar velocities are simulated for Kangerlussuaq Gletscher, although the downstream increase is not as smooth as for the Helheim Gletscher, but rather presents individual peaks between 2 and 4 km yr^{-1}. For both glaciers the ice velocity smoothly declines with time, and at end-of-simulation the peaks in ice velocity are below 2 km yr^{-1}.

In the north basin, Petermann Gletscher begins to retreat relatively late, after year 246. In the last 100 years, however, the glacier margin migrates inland by 37 kilometers, without losing contact with the ocean. The lower part of the glacier already has a negative SMB at year 140; however, during this time the SMB is slightly positive in the upper part of the glacier (0–40 km along the transect), with a gentle downstream decline to -1 m yr^{-1} at the glacier terminus. At the end of the simulation, a negative SMB of around -1 m yr^{-1} is simulated everywhere along the glacier transect. During pre-industrial, the terminus velocity peaks around 1 km yr^{-1} and declines over time, with episodic increases after margin retreats. In the same basin, Humboldt Gletscher starts retreating much earlier than Petermann, with the first retreat episode around year 184. At the end of the simulation, Humboldt has become land-terminating, with an overall margin retreat of around 60 kilometers. The SMB is already negative at year 140 over the glacier length, with a smooth gradient ranging from negative values close to zero to as low as -1 m yr^{-1} at the terminus. At the end of the simulation, the negative SMB is around -1 m yr^{-1} over the whole glacier length. At the beginning of the simulation, Humboldt Gletscher's maximum ice velocity is relatively low (700 m yr^{-1}) compared to other Greenland major drainage systems. The pattern of overall velocity decrease, with only episodic speed-ups after retreats, is also simulated for this glacier.

In the northeast basin, the Nioghalvfjerdsfjord Gletscher starts to retreat around year 159. At the end of the simulation, the glacier margin has retreated by around 46 km, with the largest part of the retreat occurring between years 270 and 350. A similar retreat of around 50 km is simulated for the Zachariae Isstrøm at year 350, although the initial retreat occurs later, around year 180. Both glaciers remain in contact with the ocean at the end of the simulation, as the fjord extends upstream by several tens of kilometers. The SMB along the flow line is negative at year 140 for both glaciers, going from negative values close to zero to values around -0.5 m yr^{-1} with a smooth gradient downstream. In the last two decades, the model simulates a negative SMB close to -1 m yr^{-1} everywhere along the transect. For both glaciers, the ice velocity near the margin peaks around 1 km yr^{-1} at pre-industrial and declines over time, although the glacier terminus velocity increases episodically after margin retreat.

In the central-west basin, Jakobshavn Isbræ starts to retreat relatively late, from year 271. At the end of the simulation, the glacier margin has retreated by only 20 km. At year 140 the SMB is negative everywhere along the glacier length, with a relatively sharp downstream gradient from slightly negative values inland to values below -1 m yr^{-1} at the glacier terminus. At the end of the simulation, the SMB has become negative over the whole glacier length, ranging downstream between -1 and -2 m yr^{-1}. At pre-industrial, simulated ice velocities are larger than 1 km yr^{-1} in the lower part of the glacier, with a sharp peak reaching 4 km yr^{-1} at the glacier terminus. In particular, ice velocities larger than 1 km yr^{-1} are found downstream of a local high in the bedrock, after which the bedrock topography is more steep. Similarly to other glaciers, the overall velocity decreases with time, with episodic speed-ups after margin retreats. At the end of the simulation, peaks in ice velocity are lower than 2 km yr^{-1}.

In summary (Supplementary Table 3), the sensitivity of these major outlet glaciers to the simulated climate change is heterogeneous, with the relatively slower, drier-basin-draining northern glaciers retreating the most, and the relatively faster, wetter-basin-draining southeastern glaciers not retreating by the end of the simulation. Of the northern glaciers, Humboldt retreats the most (60 km) and, of the total seven glaciers, is the only one that becomes terrestrial. Petermann retreats the latest. Jakobshavn Isbrae, in the central-west, retreats the least and later than the average of the northern glaciers.

3.5 GrIS Freshwater Budget

In the following, we compare the NAMOC evolution (Figure 3) with the evolution of the freshwater flux from the GrIS (Figure S6). We do this to tentatively explore a causal relationship between the simulated strong NAMOC decline and the accelerated melt over the GrIS, in the absence of a conclusive "paired" one-way coupled simulation that isolates the role of the bi-directional coupling (as in e.g., Mikolajewicz et al. (2007)). Two freshwater fluxes are considered: from ice sheet runoff and from ice discharge. For details on how these fluxes are calculated and coupled with the ocean model, see Muntjewerf et al. (in preparation). The solid freshwater flux (primarily from ice discharge) decreases during the simulation, as analyzed in previous sections 3.2 and 3.4. From approximately year 110, the liquid freshwater flux (from surface runoff and basal melt) accelerates, in connection with the melt and mass loss acceleration reported in previous sections. At this time, the magnitude of the runoff is less than 0.3×10^5 m^3 s^{-1}, but the NAMOC index has already declined to below 10 Sv. The NAMOC decline is initiated before year 50, at a time where the melt signal has not yet emerged from background variability. By end-of-simulation, runoff reaches values in excess of 0.8×10^5 m^3 s^{-1}, and the NAMOC index has stayed at levels of around 5 Sv for almost two centuries. The spatial map of runoff indicates an increasing contribution with time of the northern basins (Figure S6), as also noted in Muntjewerf et al. (submitted). The southern basins, however, remain primary contributors to the overall runoff throughout the three simulated centuries.

A similar relationship between NAMOC decline and GrIS freshwater fluxes is found under SSP5-8.5 forcing (Muntjewerf et al., submitted). In the latter study, a comparison of NAMOC index evolution with standard CESM2.1 simulations (without an interactive GrIS) under the same forcing shows similar indexes for the two cases.

3.6 Change in Greenland Summer Climate

This section examines the spatial changes in the Greenland climate for July, with a focus on temperature, albedo and turbulent heat fluxes. The GrIS loses 3% and 19% of its pre-industrial area by years 131–150 and 331—350, respectively. The model accounts for the land cover change involved in the transition from glacier to bare land or vegetation as the margins retreat. The ablation area expansion is shown in Figures 6a,b,c and S2.

In the pre-industrial summer where the ablation areas are narrow, most of the ice sheet area is covered with snow, and the total island of Greenland has a mean albedo of 0.71 (Figure8a1). More bare ice is exposed as the ablation areas widen by 131–150 and 331-150, and the overall Greenland albedo decreases to 0.64 and 0.50, respectively, from GrIS retreat and the low albedo of the expanding tundra and bare land (Figure 8a2,a3). The GrIS summer albedo decreases from 0.78 to 0.72 to 0.62 over the three periods (Table 2).

The average near-surface air temperature in pre-industrial Greenland is -4.6 °C, with lowest temperatures in the interior of the ice sheet, and highest on the south-west tundra (Figure 8b1). Mid-simulation and end-simulation, the July near-surface temperatures are above freezing on average with 1.1 °C, and 4.3 °C, respectively, although the interior maintains subfreezing air temperatures. Strong surface temperature inversions develop over the expanded ablation areas by 131–150 and 331–350 (Figure 8c2,c3). Over the expanding tundra, surface temperatures are up to 4 K higher than near-surface atmospheric temperatures.

The latent heat flux represents energy transfer due to the phase change of water, here defined as positive when directed to the surface. The sign is dependent on the humidity gradient in the surface layer, and the temperature-dependent saturation point. The pre-industrial summer latent heat flux (Figure 8d1) is of similar magnitude as the study by Ettema et al. (2010) with RACMO over the period 1958-2008: evaporation of -40 W m^{-2} over the west tundra, and sublimation of -10 W m^{-2} over the ablation zones. The summer tundra latent heat flux is negative and becomes more negative as the at the simulation progresses, meaning more evaporation as the air warms (Figure 8d1,d2,d3). The ice sheet interior latent heat flux is negative as well, indicating sublimation over heated, but non-melting areas. The ablation areas show sublimation in the pre-industrial era.

However, as the near-surface air temperature gets warmer than the surface, i.e., the temperature inversion in the surface layer develops and strengthens (Figure 8c1,c2,c3), there is deposition or condensation. It implies that moist air cools as it flows over the cold surface and reaches saturation, such that excess water vapor directly condensates (hoarfrost) or deposits on the ice. Integrated over the entire GrIS, the deposition becomes the dominating process as the melt increases and the ablation areas expand: in the time series of GrIS summer latent heat (Figure 5b, red line), the flux sign changes from negative (sublimation) to positive (deposition). Note that deposition helps the melt flux as it provides extra energy to the surface (Figure 5b, black line), but little extra mass.

The sensible heat flux represents energy transfer associated with warming and cooling of the surface, also defined as positive when directed to the surface. The sensible heat flux over the tundra is negative: the tundra warms the near-surface air (Figure 8e1,e2,3). As more tundra area is exposed over the course of the simulation, this signal extends area-wise. The ice-sheet interior sensible heat flux is negative as well, indicating warming or the air, though smaller in magnitude than over the tundra. Figure 8c1,c2,c3 indeed shows the atmospheric boundary layer in the interior is colder than the ice sheet surface throughout the simulation. In the ice sheet margins, the sensible heat flux is positive. Here, the air is warmer than the ice, leading to heating of the surface. The margin surface heat flux becomes more positive during the simulation, and maps well with the increase in surface layer temperature inversion (Figure 8c1,c2,c3) and expansion of the ablation areas. This is the dominating process of the increase in the time series of GrIS summer latent heat (Figure 5b, green line).

4 Discussion and Conclusions

The results in this paper are placed in broader context by comparing our GrIS SLR contribution to the CMIP scenario RCP8.5 estimates, as the CO_2 concentration by 2100 is close to 4xCO_2. Vizcaíno et al. (2014) with CESM1.0 projects 55 mm SLE by year 2100 from SMB contribution only, under global warming of 3.7 K. When forcing the ice sheet model CISM1.0 with the aforementioned CESM1.0 SMB field, the ensemble average SMB + ice discharge contribution was 76 mm SLE (Lipscomb et al., 2013). In the ice sheet model study with PISM by Aschwanden et al. (2019), the SLR range by 2100 is 140–330 mm SLE for the RCP8.5 forcing, with a global mean temperature change around 5 K. The coarse resolution Earth system/ice sheet model study by Vizcaino et al. (2015)

project SLR and warming of 67 mm SLE and 4.3 K, respectively, in 2100. After 150 years when the CO_2 increase has stabilized, we project 107 mm SLE GrIS contribution to SLR and a global mean temperature increase of 5.2 K with respect to pre-industrial. These estimates are in range of the above.

The lack of ocean forcing is a limitation of this study. Discussing the effect of including forcing of ocean temperatures to the calving fronts, Fürst et al. (2015) include both ocean and surface forcing, and reach 102 mm SLE under RCP8.5. Mass loss due to enhanced ice dynamics from ocean forcing only is estimated to be an order of magnitude smaller: Price et al. (2011) find 6 mm SLE of committed dynamic mass loss from ocean forcing by 2100. Nick et al. (2013) project a dynamic contribution between 11 and 18 mm SLE by 2100 from the four largest outlet glaciers. On the other hand, studies without ocean forcing give reductions in ice discharge in 2100 under RCP8.5 relative to present day (Vizcaino et al., 2015; Ruckamp et al., 2019), illustrating the important role of the ocean. Although ocean interactions are second-order compared to SMB in terms of GrIS mass loss, the above studies suggest that ocean forcing enhances ice discharge, while ice discharge reduces in the studies without. The question remains to what the net effect is, and answering this requires the development of models with GrIS ice-ocean interactions. To improve understanding of ocean-terminus and ocean-shelf processes, the ISMIP6 stand-alone ice sheet model GrIS experiments are provided with scenario ocean boundary forcing (Slater et al., 2019) to accommodate parameterizations of marine termini retreat and submarine melt.

The strength of this study is using a coupled Earth system/ice sheet model, which is a step to bridging the gap between multi-century and multi-millennia ice sheet model SLR projections with static SMB forcing, and sub-century SMB projections from global and regional climate models. Generally on multi-century time scales, most sea-level rise is expected after the forcing stabilizes due to the system's inertia. The concept of irreversibility is rooted in the interrelated feedbacks of the Earth system. In this, Pattyn et al. (2018) see much importance in the interplay between the SMB-elevation feedback and the ice-albedo-feedback and find that a negative SMB in the northwest is a useful indicator for the irreversibility threshold. Exploring the SMB components in further detail, Noël et al. (2017) postulate that future GrIS acceleration in mass loss is to be expected due to saturating the refreezing capacity, as has been currently found the case for the detached glaciers and ice caps on Greenland.

Few studies investigate the GrIS behaviour on multi-century time scale with time-varying SMB. This either requires a long simulation with a coupled Earth system/ice sheet model, or a long ESM simulation and elaborated SMB downscaling techniques that can account for the growing divergence between the static ESM GrIS geometry, and the evolving ISM geometry. After 350 years, this study finds 1140 mm SLE GrIS contribution to SLR and a global mean temperature increase of 8.5 K. The coupled, coarse resolution, Earth system/ice sheet model study by Vizcaino et al. (2015) finds 536 mm SLE and 9.4 K in 2300. The RCP8.5 ISM extension with ESM forcing by Aschwanden et al. (2019) estimates a SLR range of 940–3740 mm SLE with around 10 K warming by 2300. Our estimates are within the above range of multi-century projections, which, as noted in Bamber et al. (2019), has more uncertainty than century-scale projections.

This paper presented the results of a multi-century (350-year) simulation of GrIS evolution under an idealized CO_2 scenario as simulated by the coupled CESM2.1-CISM2.1. The goal of this experiment design was to gain process-level understanding of GrIS mass loss. With the current observed GrIS mass loss rates, relevant questions for the near-future sea level contribution are 1) to what extent can we expect the GrIS to respond to increased atmospheric warming, and 2) what are the main processes that govern this response. The GrIS reacts nonlinearly, and with a time lag, to global warming. By the end of the transient segment, the projected GrIS contribution to global mean SLR is 107 mm SLE, with a global mean temperature anomaly of 5.3 K. The polar amplification factor is 1.6, though the GrIS amplification factor is only 1.1. The North Atlantic Meridional Overturning Circulation strongly declines, starting before the substantial increases in GrIS runoff. After another 210 years of stable, high CO_2, the total projected GrIS contribution increases tenfold to 1140 mm SLE, while the global mean temperature anomaly increases to 8.5 K. The accelerated mass loss is mainly driven by a rapidly declining SMB. Part of the SMB signal is compensated by less ice discharge, because the GrIS retreats and many of the outlet glaciers become land-terminating (final area reduction is 20%). The basal mass balance makes only a minor contribution to the total mass budget, as the model does not simulate ice shelves and sub-shelf melting.

The main finding is in the chain of processes leading up to accelerated mass loss, dominantly caused by the SMB behaviour. The SMB decreases slowly at the start of the simulation. The initial energy source for the extra melt is mainly the increased net long-wave radiation as the atmosphere warms. The SMB decline accelerates after about 100 years of CO_2 increase (-13.9 Gt yr^{-2} from years 120–226), resulting from increasingly high surface melt. By this time, the ablation areas have expanded enough to trigger the albedo feedback, and the net short-wave radiation at the surface increases. Also contributing to melt energy are the turbulent heat fluxes as the summer GrIS surface reaches widespread melt conditions and the refreezing capacity of the snow becomes saturated. The global mean temperature anomaly at the start of the accelerated mass decline is 4.2 K. The SMB stabilizes about a century after the CO_2 forcing stabilizes. At the end of the simulation, the global mean temperature is 8.5 K, 60% of the GrIS is ablation area, and the mass balance is -2350 Gt yr^{-1}. Cumulatively, the GrIS contributes 1140 mm SLE to global mean SLR.

Acknowledgments

LM, RS, MV, CEdS, MP and MS analysed the simulations, KTC performed the simulations. JF, WL, ML and WS developed the model, and MS and SB tested the ice sheet component. LM and MV wrote the manuscript, and all authors contributed to and commented on the manuscript.

LM, MP, MV, and CES acknowledge funding from the European Research Council (grant no. ERC-StG-678145-CoupledIceClim). RS acknowledges funding from the Dutch Research Council (NWO) (grant no. xxx).

The CESM2 is an open source model, available at: http://www.cesm.ucar.edu/. The CESM project is supported primarily by the National Science Foundation (NSF). This material is based upon work supported by the National Center for Atmospheric Research, which is a major facility sponsored by the NSF under Cooperative Agreement No. 1852977. Computing and data storage resources, including the Cheyenne supercomputer (`doi:10.5065/D6RX99HX`), were provided by the Computational and Information Systems Laboratory (CISL) at NCAR.

The World Climate Research Program (WGCM) Infrastructure Panel is the official CMIP document home: `https://www.wcrp-climate.org/wgcm-cmip`. The CMIP6 and ISMIP6 simulations are freely available, and accessible via the Earth System Grid Federation (ESGF) data portals `https://esgf.llnl.gov/nodes.html`.

References

Alexander, P. M., LeGrande, A. N., Fischer, E., Tedesco, M., Fettweis, X., Kelley, M., . . . Schmidt, G. A. (2019). Simulated greenland surface mass balance in the giss modele2 gcm: Role of the ice sheet surface. *Journal of Geophysical Research: Earth Surface*, *124*(3), 750-765. Retrieved from `https://agupubs.onlinelibrary.wiley.com/doi/abs/10.1029/2018JF004772` doi: 10.1029/2018JF004772

Aschwanden, A., Fahnestock, M. A., & Truffer, M. (2016). Complex greenland outlet glacier flow captured. *Nat. Commun.*, *7:10524*. doi: 10.1038/ncomms10524

Aschwanden, A., Fahnestock, M. A., Truffer, M., Brinkerhoff, D. J., Hock, R., Khroulev, C., . . . Khan, S. A. (2019). Contribution of the greenland ice sheet to sea level over the next millennium. *Science Advances*, *5*(6). Retrieved from `https://advances.sciencemag.org/content/5/6/eaav9396` doi: 10.1126/sciadv.aav9396

Bamber, J. L., Griggs, J. A., Hurkmans, R. T. W. L., Dowdeswell, J. A., Gogineni, S. P., Howat, I., . . . Steinhage, D. (2013). A new bed elevation dataset for greenland. *The Cryosphere*, *7*(2), 499–510. Retrieved from `https://www.the-cryosphere.net/7/499/2013/` doi: 10.5194/tc-7-499-2013

Bamber, J. L., Oppenheimer, M., Kopp, R. E., Aspinall, W. P., & Cooke, R. M. (2019). Ice sheet contributions to future sea-level rise from structured expert judgment. *Proceedings of the National Academy of Sciences*, *116*(23), 11195–11200. Retrieved from `https://www.pnas.org/content/116/23/11195` doi: 10.1073/pnas.1817205116

Box, J. E., Fettweis, X., Stroeve, J. C., Tedesco, M., Hall, D. K., & Steffen, K. (2012). Greenland ice sheet albedo feedback: thermodynamics and atmospheric drivers. *The Cryosphere*, *6*(4), 821–839. Retrieved from `http://www.the-cryosphere.net/6/821/2012/` doi: 10.5194/tc-6-821-2012

Bradley, S., et al. (in preparation). sliding paper.

Danabasoglu, G., et al. (accepted pending minor revisions). The community earth system model version 2 (cesm2). *Journal of Advances in Modeling Earth Systems*.

Edwards, T. L., Fettweis, X., Gagliardini, O., Gillet-Chaulet, F., Goelzer, H., Gregory, J. M., . . . Ritz, C. (2014). Effect of uncertainty in surface mass balance-elevation feedback on projections of the future sea level contribution of the Greenland ice sheet. *The Cryosphere*, *8*, 195–208. Retrieved from http://www.the-cryosphere.net/8/195/2014/ doi: 10.5194/tc-8-195-2014

Ettema, J., van den Broeke, M. R., van Meijgaard, E., & van de Berg, W. J. (2010). Climate of the greenland ice sheet using a high-resolution climate model â“ part 2: Near-surface climate and energy balance. *The Cryosphere*, *4*(4), 529–544. Retrieved from https://www.the-cryosphere.net/4/529/2010/ doi: 10.5194/tc-4-529-2010

Eyring, V., Bony, S., Meehl, G. A., Senior, C. A., Stevens, B., Stouffer, R. J., & Taylor, K. E. (2016). Overview of the coupled model intercomparison project phase 6 (cmip6) experimental design and organization. *Geoscientific Model Development*, *9*(5), 1937–1958. Retrieved from https://www.geosci-model-dev.net/9/1937/2016/ doi: 10.5194/gmd-9-1937-2016

Fettweis, X., Box, J. E., Agosta, C., Amory, C., Kittel, C., Lang, C., … Gallée, H. (2017). Reconstructions of the 1900–2015 greenland ice sheet surface mass balance using the regional climate mar model. *The Cryosphere*, *11*(2), 1015–1033. Retrieved from https://www.the-cryosphere.net/11/1015/2017/ doi: 10.5194/tc-11-1015-2017

Fürst, J. J., Goelzer, H., & Huybrechts, P. (2015). Ice-dynamic projections of the greenland ice sheet in response to atmospheric and oceanic warming. *The Cryosphere*, *9*(3), 1039–1062. Retrieved from https://www.the-cryosphere.net/9/1039/2015/ doi: 10.5194/tc-9-1039-2015

Fyke, J., Sergienko, O., Lofverstrom, M., Price, S., & Lenaerts, J. T. M. (2018). An overview of interactions and feedbacks between ice sheets and the earth system. *Reviews of Geophysics*, *56*(2), 361-408. Retrieved from https://agupubs.onlinelibrary.wiley.com/doi/abs/10.1029/2018RG000600 doi: 10.1029/2018RG000600

Fyke, J. G., Vizcaino, M., & Lipscomb, W. H. (2014). The pattern of anthropogenic signal emergence in greenland ice sheet surface mass balance. *Geophysical Research Letters*, *41*(16), 6002–6008. Retrieved from http://dx.doi.org/10.1002/2014GL060735 doi: 10.1002/2014GL060735

Goelzer, H., Huybrechts, P., Furst, J., Nick, F., Andersen, M., Edwards, T., … Shannon, S. (2013). Sensitivity of greenland ice sheet projections to model formulations. *Journal of Glaciology*, *59*(216), 733–749. doi: 10.3189/2013JoG12J182

Goelzer, H., Robinson, A., Seroussi, H., & van de Wal, R. S. (2017, Dec 01). Recent progress in greenland ice sheet modelling. *Current Climate Change Reports*, *3*(4), 291–302. Retrieved from `https://doi.org/10.1007/s40641-017-0073-y` doi: 10.1007/s40641-017-0073-y

Goldberg, D. N. (2011). A variationally derived, depth-integrated approximation to a higher-order glaciological flow model. *Journal of Glaciology*, *57*(201), 157–170. doi: 10.3189/002214311795306763

Gregory, J., & Huybrechts, P. (2006). Ice-sheet contributions to future sea-level change. *Philosophical Transactions of the Royal Society A: Mathematical, Physical and Engineering Sciences*, *364*(1844), 1709-1732. Retrieved from `https://royalsocietypublishing.org/doi/abs/10.1098/rsta.2006.1796` doi: 10.1098/rsta.2006.1796

Hanna, E., Pattyn, F., Navarro, F., Favier, V., Goelzer, H., van den Broeke, M. R., … Smith, B. (2020). Mass balance of the ice sheets and glaciers â progress since ar5 and challenges. *Earth-Science Reviews*, *201*, 102976. Retrieved from `http://www.sciencedirect.com/science/article/pii/S0012825219303848` doi: https://doi.org/10.1016/j.earscirev.2019.102976

Helsen, M. M., van de Wal, R. S. W., Reerink, T. J., Bintanja, R., Madsen, M. S., Yang, S., … Zhang, Q. (2017). On the importance of the albedo parameterization for the mass balance of the greenland ice sheet in ec-earth. *The Cryosphere*, *11*(4), 1949–1965. Retrieved from `https://www.the-cryosphere.net/11/1949/2017/` doi: 10.5194/tc-11-1949-2017

Hunke, E., Lipscomb, W., Jones, P., Turner, A., Jeffery, N., & Elliott, S. (2017, 5). *Cice, the los alamos sea ice model, version 00.* Retrieved from `https://www.osti.gov//servlets/purl/1364126`

Lawrence, D. M., Fisher, R. A., Koven, C. D., Oleson, K. W., Swenson, S. C., Bonan, G., … Zeng, X. (2019). The community land model version 5: Description of new features, benchmarking, and impact of forcing uncertainty. *Journal of Advances in Modeling Earth Systems*, *n/a*(n/a). Retrieved from `https://agupubs.onlinelibrary.wiley.com/doi/abs/10.1029/2018MS001583` doi: 10.1029/2018MS001583

Lin, S.-J., & Rood, R. B. (1997). An explicit flux-form semi-lagrangian shallow-water model on the sphere. *Quarterly Journal of the Royal Meteorological Society*, *123*(544), 2477-2498. Retrieved from https://rmets.onlinelibrary.wiley.com/doi/abs/10.1002/qj.49712354416 doi: 10.1002/qj.49712354416

Lipscomb, W. H., Fyke, J. G., VizcaÃno, M., Sacks, W. J., Wolfe, J., Vertenstein, M., ... Lawrence, D. M. (2013). Implementation and initial evaluation of the glimmer community ice sheet model in the community earth system model. *Journal of Climate*, *26*(19), 7352-7371. Retrieved from https://doi.org/10.1175/JCLI-D-12-00557.1 doi: 10.1175/JCLI-D-12-00557.1

Lipscomb, W. H., Price, S. F., Hoffman, M. J., Leguy, G. R., Bennett, A. R., Bradley, S. L., ... Worley, P. H. (2019). Description and evaluation of the community ice sheet model (cism) v2.1. *Geoscientific Model Development*, *12*(1), 387–424. Retrieved from https://www.geosci-model-dev.net/12/387/2019/ doi: 10.5194/gmd-12-387-2019

Lofverstrom, M., Fyke, J., Thayer-Calder, K., Muntjewerf, L., Vizcaino, M., Sacks, W., ... Bradley, S. (in review). An efficient ice-sheet/earth system model spin-up procedure for cesm2.1 and cism2.1: description, evaluation, and broader applicability. *Journal of Advances in Modeling Earth Systems*.

Lofverstrom, M., & Liakka, J. (2018). The influence of atmospheric grid resolution in a climate model-forced ice sheet simulation. *The Cryosphere*, *12*(4), 1499–1510. Retrieved from https://www.the-cryosphere.net/12/1499/2018/ doi: 10.5194/tc-12-1499-2018

Mikolajewicz, U., VizcaÃno, M., Jungclaus, J., & Schurgers, G. (2007). Effect of ice sheet interactions in anthropogenic climate change simulations. *Geophysical Research Letters*, *34*(18). Retrieved from https://agupubs.onlinelibrary.wiley.com/doi/abs/10.1029/2007GL031173 doi: 10.1029/2007GL031173

Morlighem, M., Williams, C. N., Rignot, E., An, L., Arndt, J. E., Bamber, J. L., ... Zinglersen, K. B. (2017). Bedmachine v3: Complete bed topography and ocean bathymetry mapping of greenland from multibeam echo sounding combined with mass conservation. *Geophysical Research Letters*, *44*(21), 11,051-11,061. Retrieved from https://agupubs.onlinelibrary.wiley.com/doi/abs/10.1002/2017GL074954 doi: 10.1002/2017GL074954

Muntjewerf, L., Petrini, M., Vizcaino, M., Ernani da Silva, C., Sellevold, R., Scherrenberg, M. D. W., ... Lofverstrom, M. (submitted). Greenland ice sheet contribution to 21st century sea level rise as simulated by the coupled cesm2.1-cism2.1. *Geophysical Research Letters*.

Muntjewerf, L., Sacks, W. J., Lofverstrom, M., Fyke, J., Lipscomb, W. H., Ernani da Silva, C., ... Lenaerts, J. T. M. (in preparation). Description and demonstration of the coupled community earth system model v2.1 - community ice sheet model v2.1 (cesm2.1-cism2.1). *Journal of Advances in Modeling Earth Systems*.

Neale, R. B., & Co-authors. (in review). The ncar community atmosphere model version 6 (cam6): Scientific configuration and simulation fidelity. *J. Adv. Model. Earth Syst.*.

Nick, F. M., Vieli, A., Andersen, M. L., Joughin, I., Payne, A., Edwards, T. L., ... van de Wal, R. S. W. (2013). Future sea-level rise from greenland's main outlet glaciers in a warming climate. *Nature*, *497*(7448), 235–238. Retrieved from `https://doi.org/10.1038/nature12068` doi: 10.1038/nature12068

Noël, B., van de Berg, W. J., Lhermitte, S., Wouters, B., Machguth, H., Howat, I., ... van den Broeke, M. R. (2017). A tipping point in refreezing accelerates mass loss of greenland's glaciers and ice caps. *Nature Communications*, *8*(1), 14730. Retrieved from `https://doi.org/10.1038/ncomms14730` doi: 10.1038/ncomms14730

Noël, B., van de Berg, W. J., Machguth, H., Lhermitte, S., Howat, I., Fettweis, X., & van den Broeke, M. R. (2016). A daily, 1 km resolution data set of downscaled greenland ice sheet surface mass balance (1958–2015). *The Cryosphere*, *10*(5), 2361–2377. Retrieved from `https://www.the-cryosphere.net/10/2361/2016/` doi: 10.5194/tc-10-2361-2016

Noël, B., van de Berg, W. J., van Meijgaard, E., Kuipers Munneke, P., van de Wal, R. S. W., & van den Broeke, M. R. (2015). Evaluation of the updated regional climate model racmo2.3: summer snowfall impact on the greenland ice sheet. *The Cryosphere*, *9*(5), 1831–1844. Retrieved from `https://www.the-cryosphere.net/9/1831/2015/` doi: 10.5194/tc-9-1831-2015

Noël, B., van de Berg, W. J., van Wessem, J. M., van Meijgaard, E., van As, D., Lenaerts, J. T. M., ... van den Broeke, M. R. (2018). Modelling the climate and surface mass balance of polar ice sheets using racmo2 – part 1: Greenland (1958–2016). *The Cryosphere*, *12*(3), 811–831. Retrieved from https://www.the-cryosphere.net/12/811/2018/ doi: 10.5194/tc-12-811-2018

Nowicki, S. M. J., Payne, A., Larour, E., Seroussi, H., Goelzer, H., Lipscomb, W., … Shepherd, A. (2016). Ice sheet model intercomparison project (ismip6) contribution to cmip6. *Geoscientific Model Development*, *9*(12), 4521–4545. Retrieved from https://www.geosci-model-dev.net/9/4521/2016/ doi: 10.5194/gmd-9-4521-2016

Oerlemans, J. (1981). Some basic experiments with a vertically-integrated ice sheet model. *Tellus*, *33*, 1-11.

Pattyn, F., Ritz, C., Hanna, E., Asay-Davis, X., DeConto, R., Durand, G., … van den Broeke, M. (2018). The greenland and antarctic ice sheets under 1.5 °c global warming. *Nature Climate Change*, *8*(12), 1053–1061. Retrieved from https://doi.org/10.1038/s41558-018-0305-8 doi: 10.1038/s41558-018-0305-8

Pollard, D. (2010). A retrospective look at coupled ice sheet–climate modeling. *Climatic Change*, *100*(1), 173–194. Retrieved from http://dx.doi.org/10.1007/s10584-010-9830-9 doi: 10.1007/s10584-010-9830-9

Price, S. F., Payne, A. J., Howat, I. M., & Smith, B. E. (2011). Committed sea-level rise for the next century from greenland ice sheet dynamics during the past decade. *Proceedings of the National Academy of Sciences*, *108*(22), 8978–8983. Retrieved from https://www.pnas.org/content/108/22/8978 doi: 10.1073/pnas.1017313108

Ridley, J. K., Huybrechts, P., Gregory, J. M., & Lowe, J. A. (2005). Elimination of the greenland ice sheet in a high co2 climate. *Journal of Climate*, *18*(17), 3409-3427. Retrieved from https://doi.org/10.1175/JCLI3482.1 doi: 10.1175/JCLI3482.1

Ruckamp, M., Greve, R., & Humbert, A. (2019). Comparative simulations of the evolution of the greenland ice sheet under simplified paris agreement scenarios with the models sicopolis and issm. *Polar Science*, *21*, 14 - 25. Retrieved from http://www.sciencedirect.com/science/article/pii/S1873965218301403 (ISAR-5/ Fifth International Symposium on Arctic Research) doi: https://

doi.org/10.1016/j.polar.2018.12.003

Rybak, O., Volodin, E., Morozova, P., & Nevecherja, A. (2018, Mar 06). Incorporation of ice sheet models into an earth system model: Focus on methodology of coupling. *Journal of Earth System Science*, *127*(2), 28. Retrieved from https://doi.org/10.1007/s12040-018-0930-7 doi: 10.1007/s12040-018-0930-7

Sellevold, R., van Kampenhout, L., Lenaerts, J. T. M., Noël, B., Lipscomb, W. H., & Vizcaino, M. (2019). Surface mass balance downscaling through elevation classes in an earth system model: analysis, evaluation and impacts on the simulated climate. *The Cryosphere Discussions*, *2019*, 1–25. Retrieved from https://www.the-cryosphere-discuss.net/tc-2019-122/ doi: 10.5194/tc-2019-122

Sellevold, R., & Vizcaino, M. (submitted). Global warming threshold and mechanisms for greenland ice sheet surface mass loss. *Journal of Advances in Modeling Earth Systems*.

Shepherd, A., Ivins, E., Rignot, E., Smith, B., van den Broeke, M., Velicogna, I., ... Team, T. I. (2019). Mass balance of the greenland ice sheet from 1992 to 2018. *Nature*. Retrieved from https://doi.org/10.1038/s41586-019-1855-2 doi: 10.1038/s41586-019-1855-2

Slater, D. A., Felikson, D., Straneo, F., Goelzer, H., Little, C. M., Morlighem, M., ... Nowicki, S. (2019). 21st century ocean forcing of the greenland ice sheet for modeling of sea level contribution. *The Cryosphere Discussions*, *2019*, 1–34. Retrieved from https://www.the-cryosphere-discuss.net/tc-2019-222/ doi: 10.5194/tc-2019-222

Smith, R., Jones, P., Briegleb, B., Bryan, F., Danabasoglu, G., Dennis, J., ... Yeager, S. (2010). The parallel ocean program (pop) reference manual: Ocean component of the community climate system model (ccsm). *LANL, Tech. Report, LAUR-10-01853*.

Sun, Q., Whitney, M. M., Bryan, F. O., & heng Tseng, Y. (2017). A box model for representing estuarine physical processes in earth system models. *Ocean Modelling*, *112*, 139 - 153. Retrieved from http://www.sciencedirect.com/science/article/pii/S146350031730029X doi: https://doi.org/10.1016/j.ocemod.2017.03.004

van Angelen, J. H., M. Lenaerts, J. T., van den Broeke, M. R., Fettweis, X., & van Meijgaard, E. (2013). Rapid loss of firn pore space accelerates 21st century greenland mass loss. *Geophysical Research Letters*, *40*(10), 2109-2113. Retrieved from `https://agupubs.onlinelibrary.wiley.com/doi/abs/10.1002/grl.50490` doi: 10.1002/grl.50490

van den Broeke, M. R., Enderlin, E. M., Howat, I. M., Kuipers Munneke, P., Noël, B. P. Y., van de Berg, W. J., ... Wouters, B. (2016). On the recent contribution of the greenland ice sheet to sea level change. *The Cryosphere*, *10*(5), 1933–1946. Retrieved from `https://www.the-cryosphere.net/10/1933/2016/` doi: 10.5194/tc-10-1933-2016

Van Kampenhout, L., Lenaerts, J. T. M., Lipscomb, W., Vizcaino, M., Lhermitte, S., W., S., & Van Den Broeke, M. R. (accepted). Greenland ice sheet climate and surface mass balance in cesm2. *Journal of Geophysical Research: Earth Surface*.

van Kampenhout, L., Lenaerts, J. T. M., Lipscomb, W. H., Sacks, W. J., Lawrence, D. M., Slater, A. G., & van den Broeke, M. R. (2017). Improving the representation of polar snow and firn in the community earth system model. *Journal of Advances in Modeling Earth Systems*, *9*(7), 2583-2600. Retrieved from `https://agupubs.onlinelibrary.wiley.com/doi/abs/10.1002/2017MS000988` doi: 10.1002/2017MS000988

van Kampenhout, L., Rhoades, A. M., Herrington, A. R., Zarzycki, C. M., Lenaerts, J. T. M., Sacks, W. J., & van den Broeke, M. R. (2019). Regional grid refinement in an earth system model: impacts on the simulated greenland surface mass balance. *The Cryosphere*, *13*(6), 1547–1564. Retrieved from `https://www.the-cryosphere.net/13/1547/2019/` doi: 10.5194/tc-13-1547-2019

Vizcaino, M. (2014). Ice sheets as interactive components of Earth System Models: progress and challenges. *Wiley Interdisciplinary Reviews: Climate Change*, *5*(4), 557–568. Retrieved from `http://dx.doi.org/10.1002/wcc.285` doi: 10.1002/wcc.285

Vizcaíno, M., Lipscomb, W., Sacks, W., van Angelen, J., Wouters, B., & van den Broeke, M. (2013). Greenland surface mass balance as simulated by the Community Earth System Model. Part I: model evaluation and 1850-2005 results.

Journal of Climate, *26*, 7793–7812. doi: 10.1175/JCLI-D-12-00615.1

Vizcaíno, M., Lipscomb, W., Sacks, W., & van den Broeke, M. (2014). Greenland surface mass balance as simulated by the Community Earth System Model. Part II: 21st century changes. *Journal of Climate*, *27*, 215–226. doi: 10.1175/JCLI-D-12-00588.1

Vizcaino, M., Mikolajewicz, U., Ziemen, F., Rodehacke, C. B., Greve, R., & van den Broeke, M. R. (2015). Coupled simulations of greenland ice sheet and climate change up to a.d. 2300. *Geophysical Research Letters*, *42*(10), 3927-3935. Retrieved from https://agupubs.onlinelibrary.wiley.com/doi/abs/10.1002/2014GL061142 doi: 10.1002/2014GL061142

Table 1. Annual rate of GrIS mass loss (mm SLE yr^{-1}), cumulative GrIS mass loss (mm SLE), mass balance components (Gt yr^{-1}), and GrIS area (10^6 km^2). Mass Balance = Surface Mass Balance – Ice Discharge + Basal Melt Balance. Three time periods are shown, corresponding to pre-Industrial (years 1-300) and 1% simulations (years 131–150 and 331–350). Values are time-average [with standard deviation between square brackets if applicable].

	Pre-industrial	Years 131–150	Years 331–350
Annual mass loss	0.03 [0.23]	2.16 [0.47]	6.58 [1.04]
Cumulative mass loss	11	107	1140
MB	-13 [84]	-764 [160]	-2350 [358]
SMB	585 [85]	-367 [166]	-2259 [357]
ID	574 [5]	378 [26]	77 [8]
BMB	-24 [0]	-19 [4]	-14 [0]
GrIS area	1.966	1.918	1.598

Table 2. Summer GrIS-averaged albedo (-), near-surface temperature and skin temperature (°C), incoming short-wave radiation at the surface, incoming long-wave radiation at the surface, and surface energy balance components (W m^{-2}) (mean [standard deviation]). Melt energy = net short-wave radiation SW_{net} + net long-wave radiation LW_{net} + sensible heat flux SHF + latent heat flux LHF + ground heat flux GHF. All changes in the mean are significant ($p < 0.05$)

	Pre-industrial	Years 131–150	Years 331–350
Albedo	0.78 [0.01]	0.72 [0.01]	0.62 [0.01]
T_{2m}	-7.1 [0.8]	-1.5 [0.5]	0.6 [0.3]
T_{skin}	-7.6 [0.8]	-2.3 [0.4]	-0.8 [0.2]
SW_{in}	289.6 [3.7]	264.4 [5.2]	252.6 [6.2]
LW_{in}	231.3 [3.7]	266.6 [3.5]	279.7 [3.4]
Melt energy	8.2 [2.0]	38.2 [5.0]	83.1 [9.1]
SW_{net}	62.5 [2.3]	71.3 [3.4]	91.4 [4.4]
LW_{net}	-49.8 [2.0]	-37.7 [2.7]	-31.4 [2.8]
SHF	5.0 [1.0]	9.6 [1.9]	20.8 [2.9]
LHF	-7.8 [0.4]	-6.3 [1.0]	2.1 [2.1]
GHF	-1.7 [0.3]	1.2 [0.5]	0.2 [0.4]

Table 3. Annual ice sheet integrated surface mass balance and components mean [standard deviation] and anomalies of the mean with respect to pre-industrial (Gt yr^{-1}). SMB [1°] values are calculated as the sum of components as calculated in CLM. SMB [4 km] values are in CISM, after downscaling and remapping. SMB [1°] = snowfall + refreezing - melt - sublimation. Rain (%) = rain * 100 / (snowfall + rain). Refreezing (%) = refreezing * 100 / (rain + melt). All changes is the mean are significant ($p < 0.05$) except snowfall by 131–150. Differences with the downscaled SMB used by CISM2.1 (Table 1) are due to mass definition across components, for mass conservation purposes (see, e.g., Vizcaino et al., 2013).

Component	Pre-industrial	Years 131–150		Years 331–350	
		Absolute	Anomaly	Absolute	Anomaly
SMB [4 km]	585 [85]	-367 [166]	-952	-2259 [357]	-2844
SMB [1°]	544 [103]	-521 [217]	-1065	-2589 [442]	-3133
Precipitation	846 [83]	986 [97]	140	1122 [97]	276
Snowfall	780 [80]	750 [74]	-30*	683 [71]	-97
Rain	72 [12]	235 [38]	163	439 [59]	367
Refreezing	223 [54]	693 [73]	470	534 [43]	311
Melt	415 [92]	1,914 [251]	1499	3,804 [443]	3389
Sublimation	45 [4]	50 [6]	5	3 [11]	-42
Rain (%)	8 [1]	24 [3]	16	39 [4]	31
Refreezing (%)	46 [4]	32 [3]	-14	13 [1]	-33

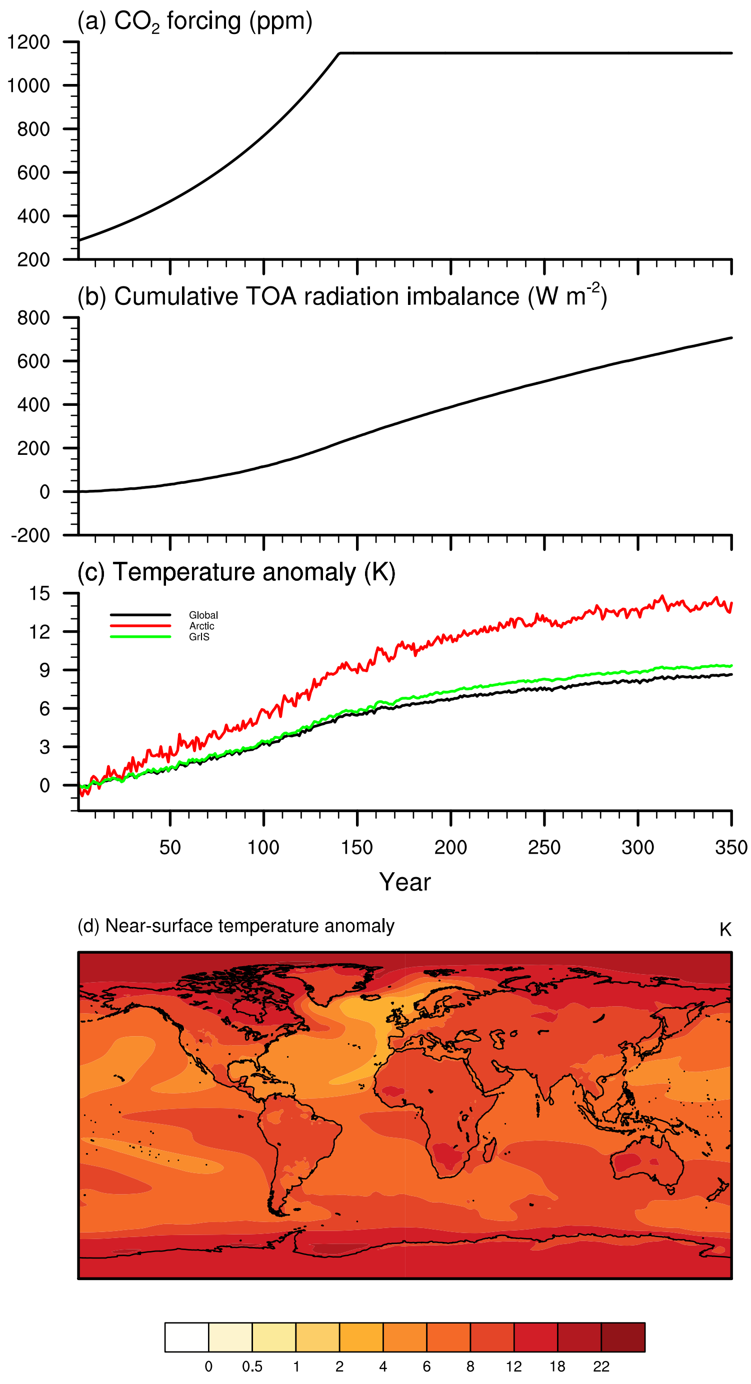

Figure 1. Evolution of (a) CO_2 (ppmv), (b) cumulative top-of-the-atmosphere (TOA) radiation imbalance, (c) near-surface temperature anomaly with respect to pre-industrial mean, and (d) anomaly map of near-surface temperature anomalies. The black lines show global averages, the red line shows Arctic (60°N-90°N) average, and the green line shows GrIS average. The anomaly map in (d) shows the difference between year 331–350 of the 4xCO_2 run and the CTRL.

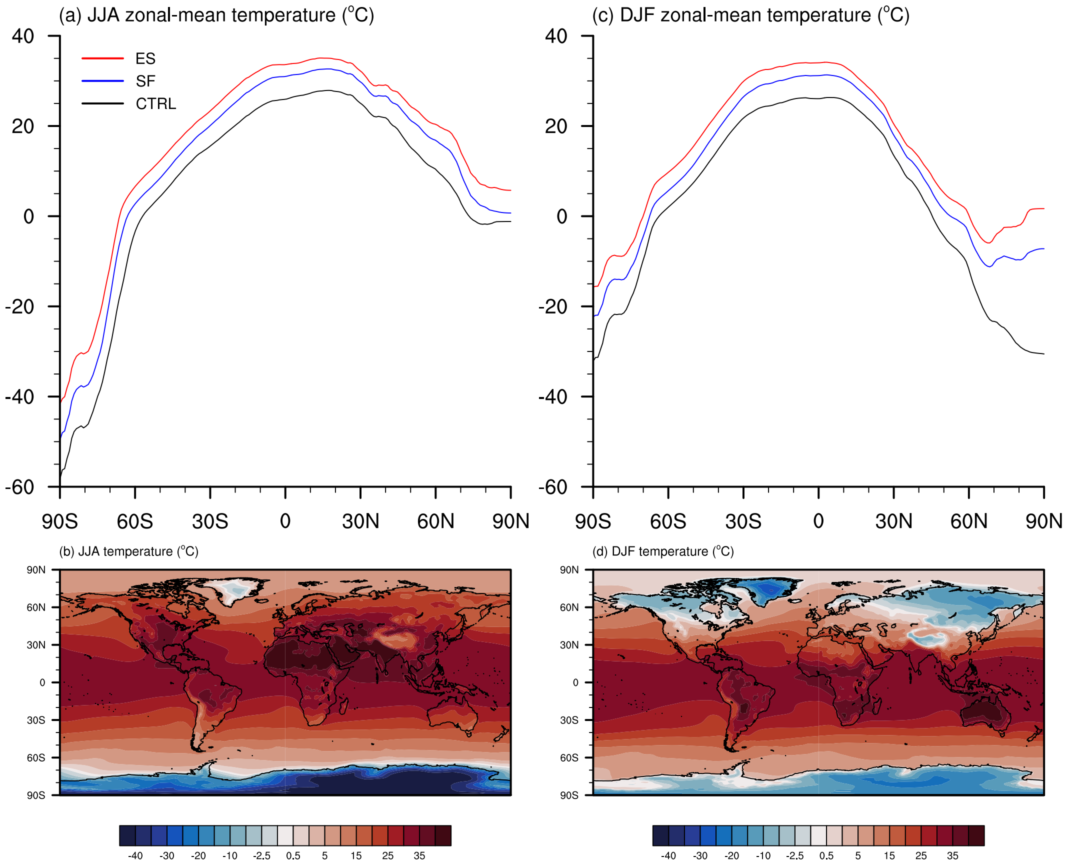

Figure 2. Zonal-mean (top) and maps (bottom) of summer (JJA; left) and winter (DJF; right) near-surface temperature (°C). The maps show the seasonal averages end-of-simulation (years 331–350).

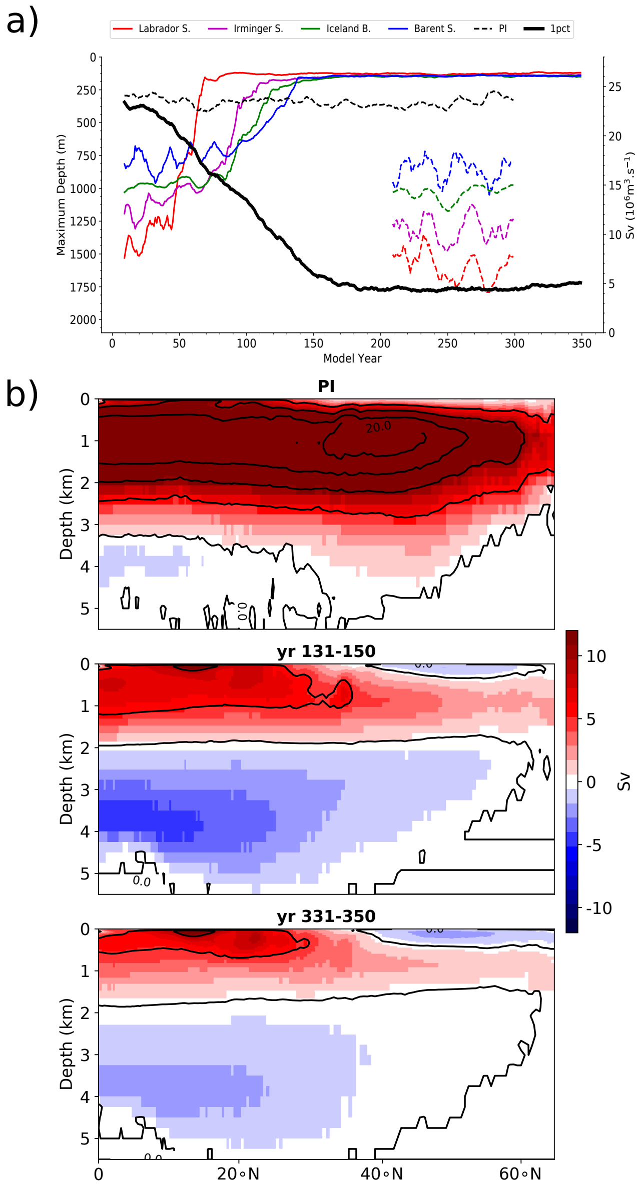

Figure 3. a) Evolution of mean January-February-March mixed layer depth at the local maximum within four regions: Labrador Sea (red), Irminger Sea (black), Iceland Basin (green) and Barent Sea (blue) and the NAMOC Index (Sv, black). Dashed lines represent pre-industrial. b) Mean North Atlantic Meridional stream function (Sv) for a) pre-industrial, b) years 131–150, and c) end of simulation (yrs 331–350).

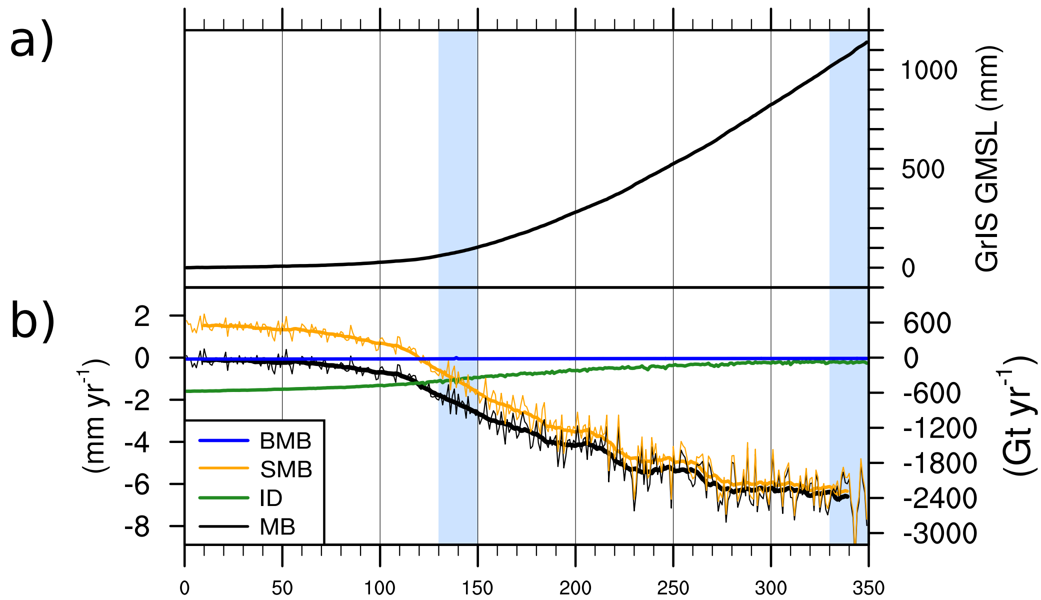

Figure 4. Cumulative (mm SLE, a) and rate (mm SLE yr^{-1} , left axis, and Gt yr^{-1}, right axis) b) GrIS contribution to global mean SLR (black, thick represents 20-year centered running mean). b) Includes the partition of mass budget in SMB (yellow), ice discharge (ID, green) and basal melt (BMB, blue) components. Note that ID and BMB are defined negative here for graphics clarity. MB = SMB + ID +BMB. Blue shade bars indicate the focused analysis periods 131–150 and 331–350.

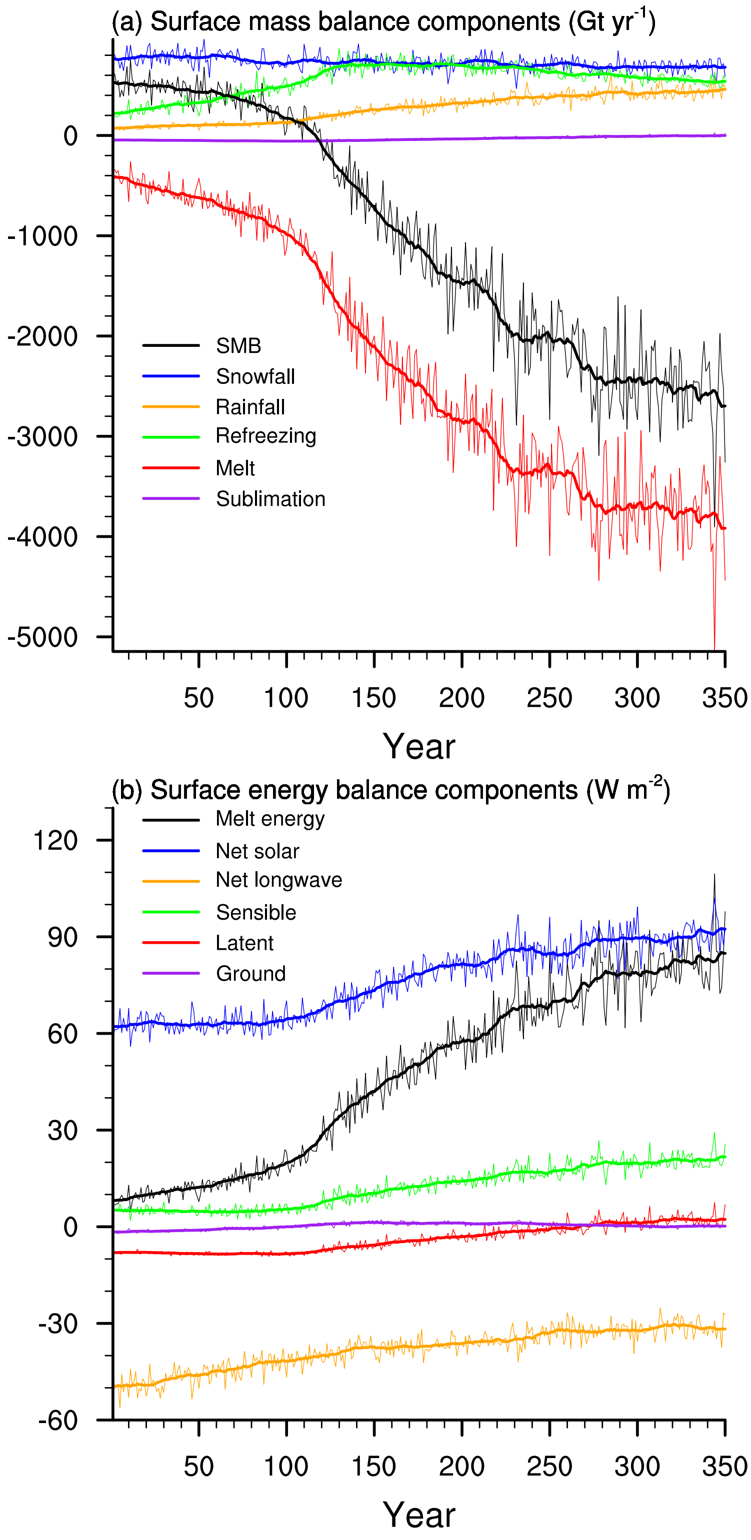

Figure 5. a) Annual GrIS-integrated SMB components (Gt yr^{-1}). Total SMB (black), snowfall (blue), rainfall (yellow), refreezing (green), melt (red), and sublimation (purple). b) GrIS mean summer SEB components (W m^{-2}). Melt energy (black), net solar radiation (blue), net longwave radiation (yellow), sensible heat flux (green), latent heat flux (red), and ground heat flux (purple). Thick lines are the running mean.

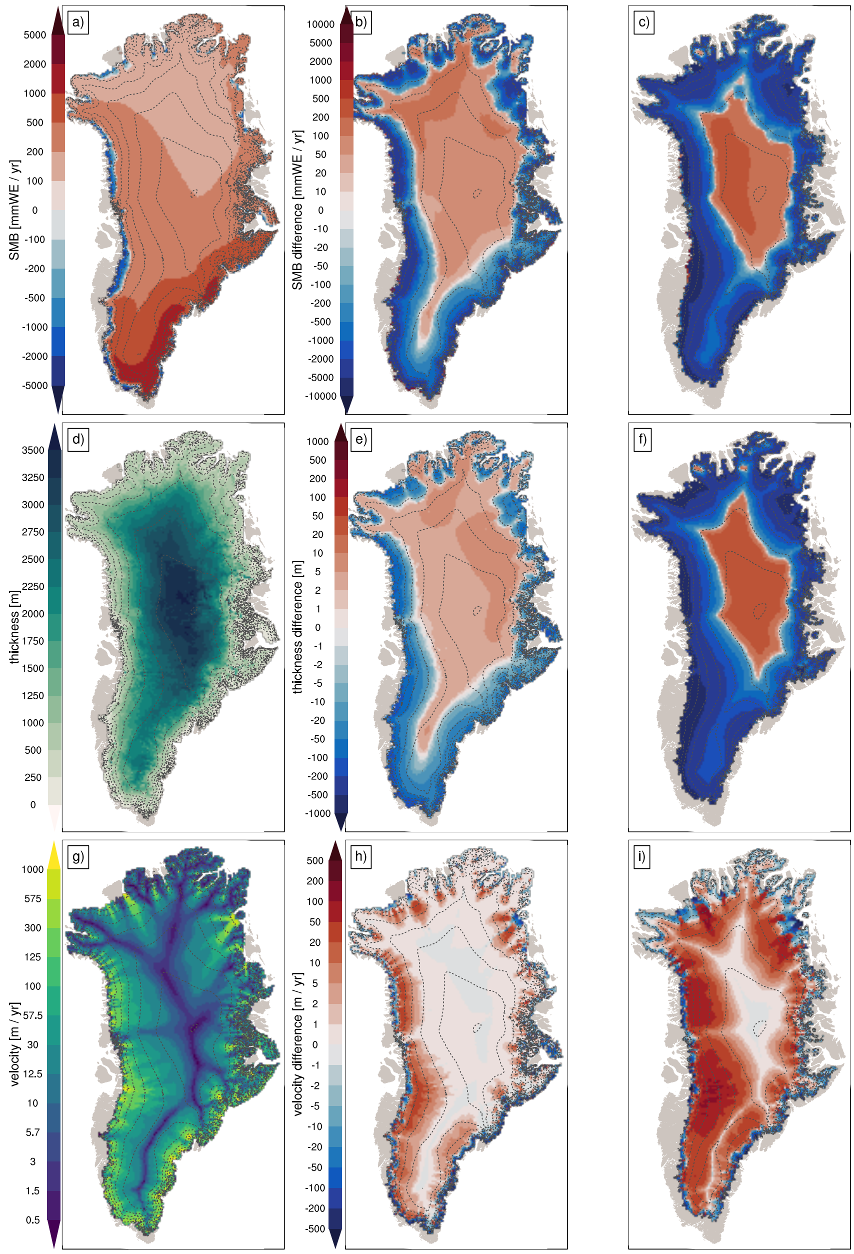

Figure 6. Spatial change over the GrIS as simulated in the ice sheet model (CISM2.1) for pre-industrial (left column) and differences w.r.t to the former by model years 131–150 (middle column) and 331–350 (right column). a) Surface mass balance (kg m^{-2} yr^{-1}) with accumulation zones: SMB > 0 and ablation zones: SMB < 0, b) ice sheet thickness (m), and c) surface velocity (m yr^{-1}).

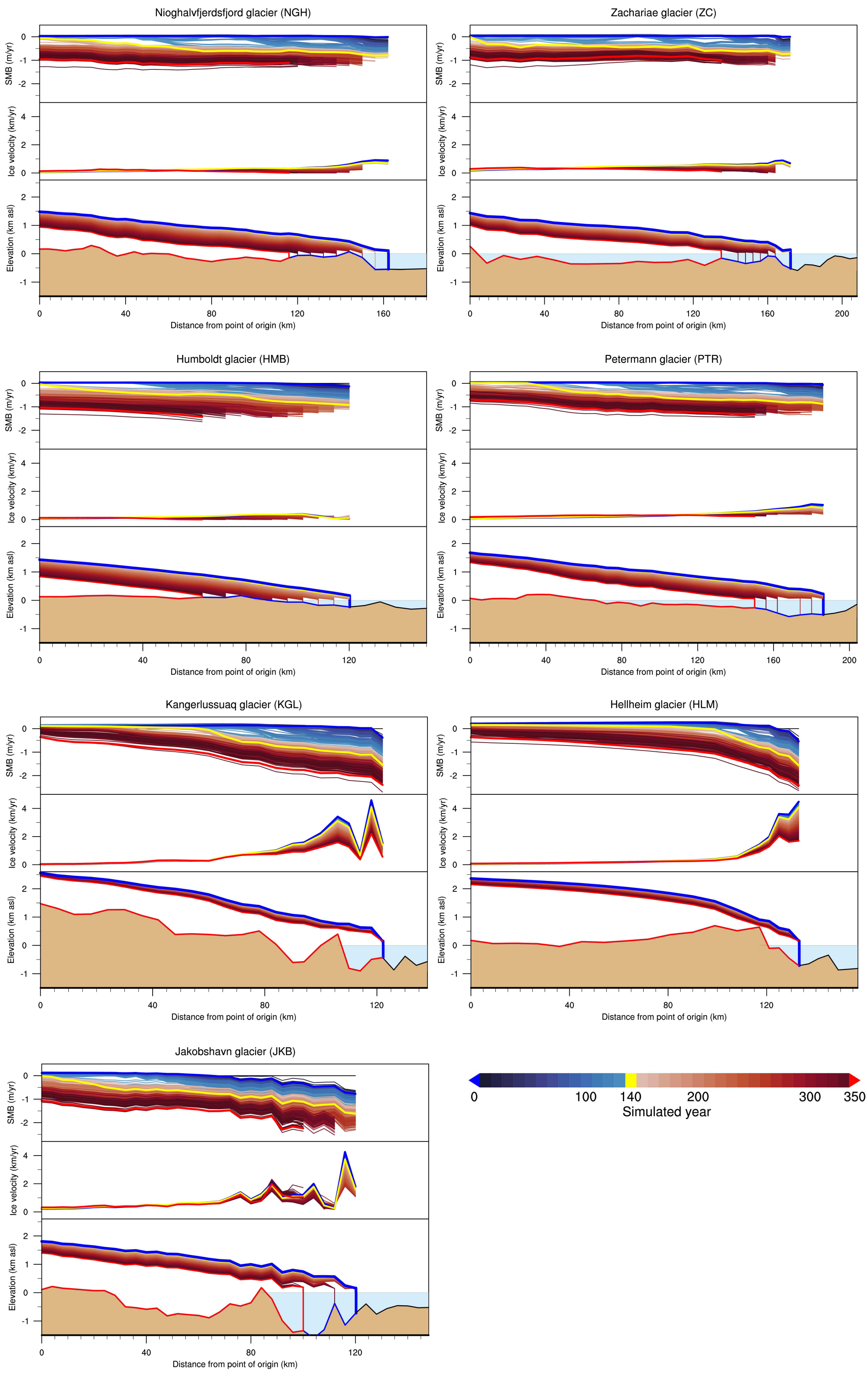

Figure 7. A flowline section of seven selected glaciers. Evolution of bottom panels): ice thickness, central panels) ice velocity, and top panels) SMB. Each line corresponds to a simulation year. Years 0, 140 and 351 are highlighted in blue, yellow and red, respectively. For clarity, different scales for ice velocity are used for different glaciers.

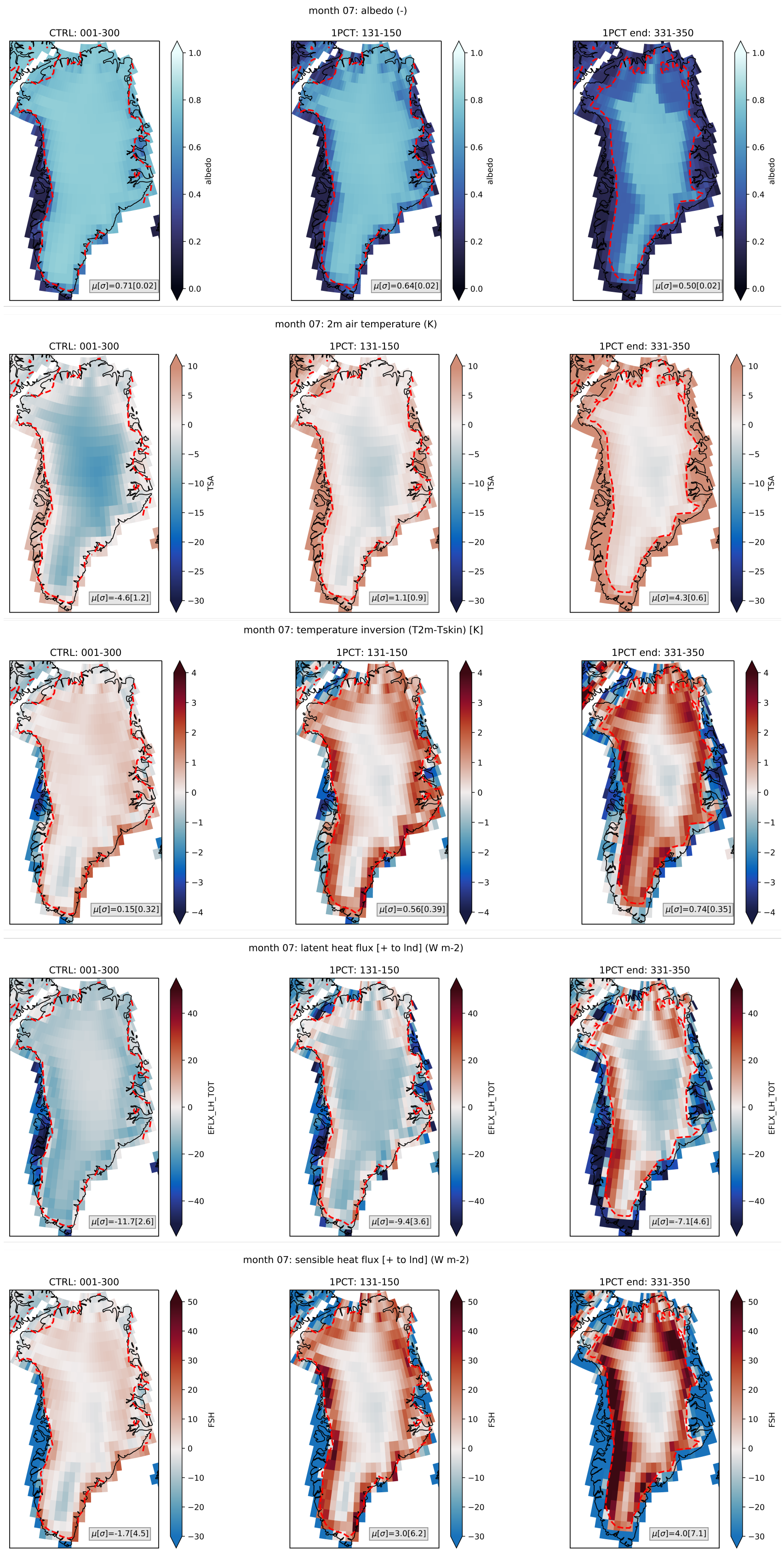

Figure 8. July Greenland climate for left) pre-industrial (1-300), middle) years 131–150 and right) 331–350, with: a) albedo (-), b) T2m (°C), c) surface temperature inversion T2m-Tskin (°C), d) latent heat flux (W m^{-2}, and e) sensible heat flux (W m^{-2}). Red contour denotes the then-current ice sheet extent, with 70% glaciated CLM grid cell area.